A&A 502, 529–540 (2009)
DOI: 10.1051/0004-6361/200911685

Astronomy & Astrophysics

New H_2O masers in Seyfert and FIR bright galaxies

III. The southern sample

G. Surcis[1,2,3], A. Tarchi[1,4], C. Henkel[3], J. Ott[5,6,⋆], J. Lovell[7], and P. Castangia[1]

[1] INAF – Osservatorio Astronomico di Cagliari, Loc. Poggio dei Pini, Strada 54, 09012 Capoterra (CA), Italy
[2] Argelander-Institut für Astronomie der Universität Bonn, Auf dem Hügel 71, 53121 Bonn, Germany
e-mail: gsurcis@astro.uni-bonn.de
[3] Max-Planck Institut für Radioastronomie, Auf dem Hügel 69, 53121 Bonn, Germany
[4] INAF-Istituto di Radioastronomia, via Gobetti 101, 40129 Bologna, Italy
[5] National Radio Astronomy Observatory, PO Box O, 1003 Lopezville Road, Socorro, NM 87801-0387, USA
[6] California Institute of Technology, 1200 E California Blvd, Caltech Astronomy 105-24, Pasadena, CA 91125, USA
[7] Department of Maths and Physics, University of Tasmania, Private Bag 21, Hobart, Tasmania 7001, Australia

Received 20 January 2009 / Accepted 30 April 2009

ABSTRACT

Context. A relationship between the water maser detection rate and far infrared (FIR) flux densities was established as a result of two 22 GHz maser surveys in a complete sample of galaxies (Dec > −30°) with 100 μm flux densities of >50 Jy and >30 Jy.
Aims. We attempted to discover new maser sources and investigate the galaxies hosting the maser spots by extending previous surveys to southern galaxies with particular emphasis on the study of their nuclear regions.
Methods. A sample of 12 galaxies with Dec < −30° and $S_{100\,\mu m}$ > 50 Jy was observed with the 70-m telescope of the Canberra deep space communication complex (CDSCC) at Tidbinbilla (Australia) in a search for water maser emission. The average 3σ noise level of the survey was 15 mJy for a 0.42 km s^{-1} channel, corresponding to a detection threshold of ∼0.1 $L_\odot$ for the isotropic maser luminosity at a distance of 25 Mpc.
Results. Two new detections are reported: a kilomaser with an isotropic luminosity $L_{H_2O} \sim 5\ L_\odot$ in NGC 3620 and a maser with about twice this luminosity in the merger system NGC 3256. The detections have been followed-up by continuum and spectral line interferometric observations with the Australia Telescope Compact Array (ATCA). In NGC 3256, a fraction (about a third) of the maser emission originates in two hot spots associated with star formation activity, which are offset from the galactic nuclei of the system. The remaining emission may originate in weaker centres of maser activity distributed over the central 50″. For NGC 3620, the water maser is coincident with the nuclear region of the galaxy. Our continuum observations indicate that the nature of the nuclear emission is probably linked to particularly intense star formation. Including the historical detection in NGC 4945, the water maser detection rate in the southern sample is 15% (3/20), consistent with the northern sample. The high rate of maser detections in the complete all-sky FIR sample (23%, 15/65) confirms the existence of a link between overall FIR flux density and maser phenomena. A relation between H_2O and OH masers in the FIR sample is also discussed.

Key words. galaxies: individual: NGC 3620, NGC 3256 – galaxies: active – galaxies: ISM – masers – radio lines: ISM – radio lines: galaxies

1. Introduction

A crucial problem in the study of active galaxies is our lack of understanding of the detailed geometry, physics, and evolution of the central engines and their environments. Another long-standing and unexplored problem is the measurement of the proper motions and geometrical distances of galaxies. In the resolution of both problems, observations of water masers at 22 GHz ($\lambda \sim 1.3$ cm) are indispensable. The rest frequency corresponds to the strongest water maser transition, the $6_{16} \rightarrow 5_{23}$ line of ortho-H_2O, which originates in dense ($n(H_2) \gtrsim 10^7$ cm^{-3}) and warm ($T_{kin} \gtrsim 400$ K) molecular gas (e.g., Henkel et al. 2005a).

Extragalactic H_2O masers are commonly classified according to their isotropic luminosity: the "megamasers" have $L_{H_2O} > 10\ L_\odot$ and the "kilomasers" have $L_{H_2O} < 10\ L_\odot$. Because of the beamed nature of the maser emission, this classification may not in every case carry significant physical meaning. However, for the sake of consistency with previous studies, we adopt the aforementioned classification throughout this paper. The "megamasers" are seen out to cosmological distances (Impellizzeri et al. 2008), and, when studied in detail, are always found to be associated with Active Galactic Nuclei (AGN) (e.g., Lo 2005). The "kilomasers" are mostly associated with star-forming regions similar to those seen in the Galaxy, although a few sources (e.g., M 51: Hagiwara et al. 2001; NGC 4051: Hagiwara et al. 2003; NGC 4151: Braatz et al. 2004) also show hints of an association with the nucleus of their host galaxies. This association is consistent with the possible presence of a buried AGN of low luminosity (LLAGN) (Hagiwara et al. 2001) and the possibility that some kilomasers also belong to the family of AGN masers, representing only the weak tail of their distribution as postulated by Ho et al. (1987).

In the past two decades, 22 GHz H_2O maser surveys of various samples of galaxies have been carried out (e.g., Henkel et al. 1986; Braatz et al. 1996 1997; Greenhill et al. 2003;

⋆ J.O. is a Jansky Fellow of the National Radio Astronomy Observatory.

Hagiwara et al. 2003; Henkel et al. 2005b (HPT); Kondratko et al. 2006; Braatz & Gugliucci 2008; Castangia et al. 2008 (CTH)). The survey of Braatz et al. (1997) consisted of 354 active galaxies, including a distance-limited sample of Seyferts and Low Ionization Nuclear Emission Regions (LINERs) with recessional velocities <7000 km s^{-1}, and a magnitude-limited sample, also including Seyferts and LINERs, with optical magnitudes of $m_B \leq 14.5$. Their 10 newly detected sources enabled them to associate the H_2O megamaser phenomenon with Seyfert 2 and LINER galaxies and not with Seyfert 1 or other types of galaxies. This indicates that the obscuring gas around an active nucleus, coupled with long gain paths along a preferentially edge-on oriented circumnuclear disk plays an important role.

Detecting more extragalactic water masers is important to tackling a number of important astrophysical problems. As previously mentioned, these sources can be used, in particular, to determine proper motions in the Local Group (Brunthaler et al. 2005, 2007), pinpoint sites of active star formation (e.g., Tarchi et al. 2002; Brunthaler et al. 2006), obtain geometrical distances, study the accretion disks surrounding AGN (Miyoshi et al. 1995; Herrnstein et al. 1999; Reid et al. 2009), and, ultimately, improve our knowledge of the equation of state of the dark energy by obtaining a high precision measurement of the Hubble constant (Braatz et al. 2008).

Since we know that far-infrared (FIR) emission commonly originates in dust grains heated by newly formed stars, a sample of FIR bright galaxies is a suitable tool for detecting extragalactic H_2O masers, in particular those associated with star-forming regions. A correlation between the presence of H_2O masers and 100 μm flux density ($S_{100\,\mu m} > 50$ Jy) was indeed reported by HPT as a result of an Effelsberg 100-m survey of all galaxies with declination Dec > −30°, associated with IRAS point sources with fluxes $S_{100\,\mu m} > 50$ Jy (Fullmer & Lonsdale 1989) (hereafter referred to as "the northern sample"). They obtained a detection rate of 22% (10/45) and found a correlation between FIR flux density and the luminosity of extragalactic maser emission. This correlation was confirmed by CTH with a complementary sample of 41 galaxies with 30 Jy $< S_{100\,\mu m} <$ 50 Jy and Dec > −30°, which yielded a detection rate of 5% in agreement with the expected value derived by the correlation. This is corroborated by the particularly sensitive study of Darling et al. (2008), which expanded the sample of known H_2O kilomasers associated with star formation and atributed the paucity of detections in the weaker tail of the extragalactic water masers mostly to the lack of sufficient sensitivity in past surveys.

The high number of detections obtained by HPT and CTH have motivated us to complement our sample by including all southern galaxies (with declination Dec < −30°) associated with IRAS point sources characterized by $S_{100\,\mu m} > 50$ Jy (hereafter referred to as "the southern sample").

2. Observations and data reduction

The list of sources in our sample, consisting of 20 galaxies, was compiled using the IRAS Point Source Catalog (Fullmer & Lonsdale 1989) and is shown in Table 1. Eight of these sources were already part of previous surveys and in the table their names are given in italics. The names of the twelve remaining sources are indicated in boldface.

2.1. Tidbinbilla data

The sources of our subsample were observed in the 6_{16}−5_{23} transition of H_2O (rest frequency: 22.23508 GHz) with the 70 m NASA Deep Space Network antenna located at Tidbinbilla[1], Australia. Our observations were made in 2005, from January to April, and in 2007, from August to September. Some sources, such as NGC 3620, were observed in both periods. The full

Table 1. Southern sample[a].

Source[b]	V-range (km s^{-1})	rms (mJy)	$L^c_{H_2O}$ ($L_\odot$)	Epoch	Tel[d]
NGC 0055	–592, 752	10	<0.001	25-Jan.-2005	T
NGC 0134	891, 2236	5	<0.08	09-Sep.-2007	T
NGC 0300	–518, 827	9	<0.001	24-Apr.-2005	T
				30-Apr.-2005	
	–547, 797	5	<0.001	17-Sep.-2007	
				18-Sep.-2007	
NGC 1097		15	<0.30	13-Aug.-2003	
NGC 1313	–262, 1083	4	<0.005	02-Jan.-2005	T
NGC 1365		12	<0.39	09-Jun.-2003	
NGC 1559	596, 1941	5	<0.05	09-Apr.-2005	T
				10-Apr.-2005	
NGC 1672		19	<0.41	27-Jun.-2004	
NGC 1792	478, 1823	5	<0.05	24-Apr.-2005	T
				30-Apr.-2005	
NGC 1808		15	<0.18	05-May-2003	
NGC 2997	353, 1697	7	<0.05	17-Apr.-2005	T
				19-Apr.-2005	
				24-Apr.-2005	
NGC 3256[e]	see Table 2				T
					A
NGC 3620[e]	see Table 2				T
					A
NGC 3621	35, 1380	5	<0.02	26-Mar.-2005	T
				02-Apr.-2005	
NGC 4945			160	20-Sep.-1978	
				22-Sep.-1978	
NGC 5128[f]	–50, 1200	–	–	10-Apr.-2005	T
				17-Apr.-2005	
				24-Apr.-2005	
	407, 668	2	<0.02	29-Jun.-2006	A
NGC 6744		15	<0.13	17-May-2002	
NGC 7552		13	<0.41	19-Jun.-2004	
NGC 7582		13	<0.40	27-Jun.-2004	
NGC 7793	–445, 899	7	<0.002	26-Aug.-2007	T
				31-Aug.-2005	

[a] For coordinates, systemic velocities, 100 μm flux densities, and references see the Table containing the entire sample of FIR bright galaxies.
[b] Bold-faced source names refer to sources observed in this study; source names in italics refer to previously measured targets. For NGC 4945, see Dos Santos & Lèpine (1979), Batchelor et al. (1982), Greenhill et al. (1997). For the other sources in italics, see Kondrakto et al. (2006).
[c] Upper limits to maser luminosities are derived from $L_{H_2O}/[L_\odot] = 0.023 \times S/[\mathrm{Jy}] \times \Delta v/[\mathrm{km\ s^{-1}}] \times D^2/[\mathrm{Mpc^2}]$, where S is 3 times the rms, in Col. 4, and Δv is the channel width, 0.5 km s^{-1} and 1.7 km s^{-1} in our Tidbinbilla and ATCA observations (NGC 5128/Cen A only), respectively.
[d] Telescope: T = Tidbinbilla; A = ATCA.
[e] Newly detected maser.
[f] Observed with ATCA, because the 22 GHz continuum was too strong to obtain single-dish spectra with high baseline quality.

[1] The Deep Space Network DSS-43 Tidbinbilla antenna is managed by the Jet Propulsion Laboratory, California Institute of Technology, under a contract with the National Aeronautics and Space Administration. Access for radio astronomy is provided through an arrangement between the Australian and US governments and is coordinated by the CSIRO Australia Telescope National Facility.

width at half maximum (*FWHM*) beamwidth was ≈50″ and the pointing accuracy was of higher quality than 20″. In both periods, observations were made with the same correlator configuration consisting of two independently tuned left circular-polarized (LCP) bands, each 64 MHz wide, and providing spectra with 2048 channels per band. Observations were made in a position switching mode. The integration time (including overheads) was typically 2.5 h per galaxy, resulting in approximately 1 h on source.

Each IF covers a velocity range of ∼900 km s^{-1} with a channel spacing of 0.42 km s^{-1}. The two IFs are centred on slightly different central frequencies, with a frequency separation of ∼50 MHz, leading to an overlap between the IFs of about 300 km s^{-1}. In this way, we could sample a total velocity range of ∼1200 km s^{-1}. All data were reduced using standard procedures of the Australia Telescope National Facility (ATNF) Spectral Analysis Package version 2.2[2] (ASAP v2.2) which is based on AIPS++ software libraries. To reduce the noise in the final spectrum, the scans of an individual undetected source were averaged, which produced a monitoring timescale of 30 days or less. To calibrate data, i.e., to convert them from Kelvin to Jansky, we used the standard equation provided by the ATNF

$$S_\nu(\mathrm{Jy}) = T_{\mathrm{source}} \cdot \chi_{\mathrm{c}} = T_{\mathrm{source}} \cdot \frac{C \cdot C_0 \cdot 0.7172}{G(el)}, \quad (1)$$

where C_0 is the opacity correction and $G(el)$ is the gain curve at 22 GHz depending on the elevation. For our observations, χ_{c} has a value of 1.75 for each period and the flux calibration uncertainty is estimated to be of order 20%. More observational details are given in Table 1.

The galaxies NGC 3256 and NGC 3620 were again observed in 2008 with the same correlator configuration. In March 2008, both IFs of NGC 3620 were centred at the maser velocity (see Sect. 3.2) covering a velocity range of ∼900 km s^{-1} with a channel spacing of 0.42 km s^{-1}. In April 2008, NGC 3256 and NGC 3620 were observed once more using the original correlator configuration covering a total of ∼1200 km s^{-1}. Eight contiguous channels were averaged in the spectra presented in Sect. 3.

2.2. ATCA data

NGC 3620 was observed in continuum and spectral line mode with the Australia Telescope Compact Array (ATCA)[3], an array of six 22-m antennas, in its most extended 6 km array configuration during average-good weather conditions in April 2006.

Continuum data were obtained simultaneously at *C* and *X*-band, i.e., at 4799.907 and 8639.948 MHz, respectively, with a standard bandwidth of 128 MHz for a total integration time of 12 h, including overheads. PKS1934-638 (5.83 Jy at 4.8 GHz and 2.84 Jy at 8.6 GHz) and PKS1057-797 (2.28 Jy and 2.20 Jy at 4.8 GHz and 8.6 GHz, respectively) were used as amplitude and phase calibrators, respectively. Line and continuum data were reduced using standard procedures of the Multichannel Image Reconstruction, Image Analysis and Display (MIRIAD) data reduction package. This includes natural weighting and deconvolution by the CLEAN algorithm (Högbom 1974).

NGC 3620 was also observed in spectral line mode at 22.100 GHz. We used the FULL_8_512_128 correlator configuration with one IF (Frequency 1) centred on the maser line with a bandwidth of 8 MHz (∼108 km s^{-1}) and 512 spectral channels (channel spacing ∼16 kHz ≈ 0.2 km s^{-1}). Simultaneously, the second IF (Frequency 2) was set to observe in continuum mode with a 128 MHz bandwidth at a central frequency of 19.5 GHz. The calibrators PKS1934-638 (0.96 Jy) and PKS1057-797 (1.73 Jy) were observed for flux and phase calibration, respectively. The source PKS1921-293 (12.67 Jy) was used to calibrate the bandpass. Standard procedures implemented in MIRIAD were used to reduce the spectral data. We subtracted the continuum by using the MIRIAD task UVLIN, which separates line and continuum in a spectral visibility data set, obtaining both a continuum-free cube and a continuum data set at 22.1 GHz.

Toward the strong continuum source NGC 5128 (Cen A), standing waves corrupted the single dish spectra during our survey at Tidbinbilla. In June 2006, we therefore observed NGC 5128 (Cen A) with the ATCA 1.5 km array configuration in spectral line mode. The data were obtained at *K*-band (22 GHz) using the FULL_32_256 correlator configuration with a single 32 MHz wide IF (432 km s^{-1}) divided into 256 channels of width 125 kHz ≈ 1.7 km s^{-1}. The sources PKS1934-638 (0.81 Jy), PKS1313-333 (1.06 Jy), and PKS1253-055 (14.02 Jy) were used as amplitude, phase, and bandpass calibrators, respectively. As described before, by using the task UVLIN, a *K*-band continuum map from the line-free channels was produced.

Finally, we observed NGC 3256 in April 2008 with the ATCA 6 km array configuration in spectral line mode at 22 GHz using the FULL_32_128-128 correlator configuration with one IF (Frequency 1), covering 32-MHz (432 km s^{-1}), all data being divided into 128 spectral channels of width 250 MHz ≈ 3.4 km s^{-1}. Simultaneously, IF2 (Frequency 2) was set to observe the continuum at 19.5 GHz with 128 MHz bandwidth. The amplitude and phase calibrators were PKS1934-638 (0.96 Jy) and PKS1004-50 (0.80 Jy), respectively. To calibrate the bandpass, we also observed PKS1921-293 (10.45 Jy). The weather was good during the entire observing session. Once again, by means of the MIRIAD task UVLIN, we produced a *K*-band continuum map from the line-free channels.

3. Results

Two new H_2O masers were detected, in the merging system NGC 3256 and in the spiral galaxy NGC 3620. Line profiles and continuum maps are shown in Figs. 1–6, while line and continuum parameters are given in Tables 2 and 3.

3.1. NGC 3256

NGC 3256 is a well studied merging galaxy located at a distance of ∼37 Mpc (1″ ∼ 180 pc; H_0 = 75 km s^{-1} Mpc^{-1}). With an IR luminosity of $L_{\mathrm{IR}} \sim 6 \times 10^{11} L_\odot$ (Lira et al. 2008), it is one of the most luminous galaxies in the nearby Universe. The galaxy consists of a main body, two extended tidal tails with a total extension of ∼80 kpc, and two faint external loops (Lípari 2000). The double tidal tails are characteristic of an interaction between two spiral galaxies of comparable mass (e.g., de Vaucouleurs & de Vaucouleurs 1961).

Two distinct nuclei aligned along a north-south axis have been identified by high spatial resolution near-IR (e.g. Kotilainen et al. 1996), MIR (Böker et al. 1997), and radio observations (e.g. Norris & Forbes 1995, hereafter NF95; Neff et al. 2003). Their projected separation is only ∼1 kpc (5″). At radio wavelengths, the two nuclei are of approximately similar

[2] http://www.atnf.csiro.au/computing/software/asap/

[3] The Australia Telescope Compact Array is part of the Australia Telescope which is funded by the Commonwealth of Australia for operation as a National Facility managed by CSIRO.

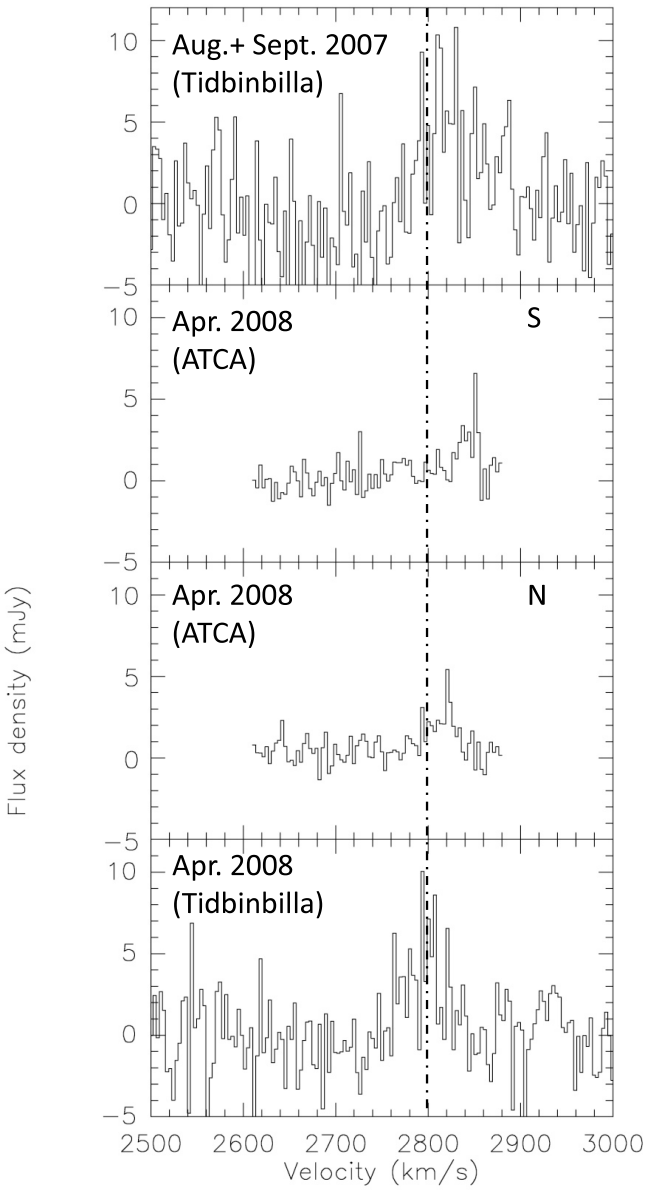

Fig. 1. H_2O maser in NGC 3256. The channel spacing and pointing position for the Tidbinbilla spectra are 3.4 km s^{-1} and $\alpha_{2000} = 10^h27^m51\overset{s}{.}3$, $\delta_{2000} = -43°54'14''$, respectively. The channel spacing for the ATCA data is 3.7 km s^{-1}, where two emission peaks have been found at different positions (N = north, S = south). The velocity scale is with respect to the local standard of rest (LSR). The recessional LSR velocity of the galaxy (the dot-dashed line) is 2799 km s^{-1} according to the NASA/IPAC database (NED).

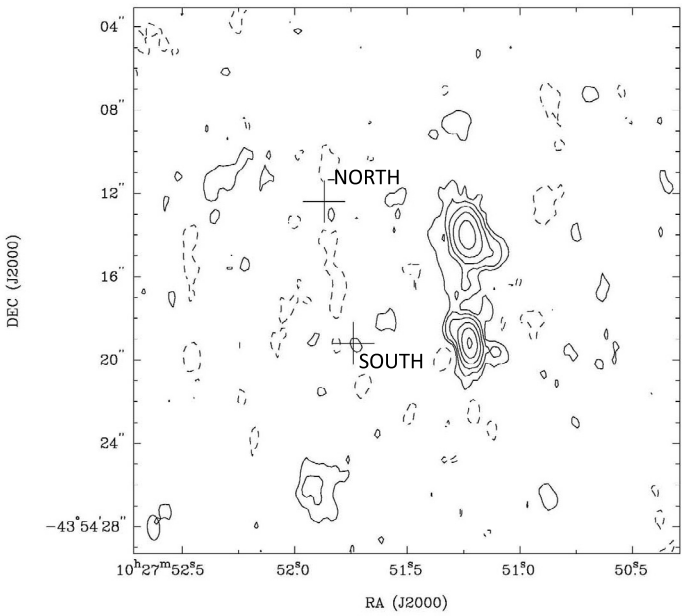

Fig. 2. Radio continuum map of the nuclear region of NGC 3256, observed with ATCA at 19.5 GHz (K-band). Contour levels are 0.3 mJy/beam(3σ) × −1 (dashed contours), 1, 2, 4, 8, 16 and 32 (solid contours). For more details see Tables 3 and 4. The crosses indicate the two maser spots observed with ATCA at 22 GHz.

size, brightness, and spectral index. These indices are quite steep ($\alpha \sim -0.8$), so that the radio continuum emission must be dominated by nonthermal synchrotron processes (NF95) typical of a starburst galaxy. There is abundant molecular gas (10^{10} $M_\odot$) in the central region surrounding the double nucleus, which presumably feeds the starburst (e.g., Sargent et al. 1989; Casoli et al. 1991). The starburst was also detected in radio recombination lines of hydrogen and helium within the central 3″ nuclear region and prominent CO band absorption at 2.3 μm (Doyon et al. 1994).

Lira et al. (2008) determined a star formation rate (SFR) of ∼15 and ∼6 $M_\odot$ yr^{-1} for the northern and southern nucleus, respectively. These SFRs are in good agreement with the values obtained by NF95 using a supernova rate of 0.3 yr^{-1} per nucleus. The data presented by Lira et al. (2008) further suggest that a significant fraction of the mid-IR excess is due to continuum emission produced by warm dust, heated in-situ by the starburst itself.

High-resolution spatial and spectral Chandra observations were analysed by Lira et al. (2002). About 80% of the X-ray emission is of diffuse origin. Each of the two nuclei is associated with one of the 14 identified discrete sources, which provide the remaining 20% of the X-ray emission. Based on a comparison of radio and X-ray observations, Neff et al. (2003) proposed the presence of a low-luminosity AGN in each nucleus, while Jenkins et al. (2004) found no strong evidence for an AGN in the X-ray data alone.

We detected water maser emission in August 2007. Figure 1 shows the detected line at different epochs, while line parameters are given in Table 2. An isotropic luminosity of ∼10 $L_\odot$ places the maser close to the limit between water kilomasers and megamasers.

In the ATCA observation, about a third of the total H_2O emission is seen to originate from two separate maser spots, a northern one (labelled N) located at $\alpha_{2000} = 10^h27^m51\overset{s}{.}87 \pm 0\overset{s}{.}01$ and $\delta_{2000} = -43°54'12\overset{''}{.}4 \pm 0\overset{''}{.}1$, and a southern one (labelled S) at $\alpha_{2000} = 10^h27^m51\overset{s}{.}74 \pm 0\overset{s}{.}01$ and $\delta_{2000} = -43°54'19\overset{''}{.}2 \pm 0\overset{''}{.}1$ (Fig. 2). Gaussian fits provide peak velocities of 2822 km s^{-1} and 2840 km s^{-1}, peak flux densities of 3.5 mJy and 2.1 mJy, and linewidths of 8 km s^{-1} and 16 km s^{-1} for the northern and southern maser, respectively. Hence, both features are redshifted with respect to the systemic velocity, by 23 km s^{-1} (N) and 41 km s^{-1} (S). The luminosities of the N and S masers are 1.0 $L_\odot$ and 2.4 $L_\odot$, respectively.

A few days after the ATCA observations, we observed the maser source again with Tidbinbilla. The peak velocity was ∼2797 km s^{-1}, the peak flux density was 10 mJy and the linewidth was 40 km s^{-1}, providing a single-dish luminosity of ∼13 $L_\odot$, slightly higher than that measured in 2007.

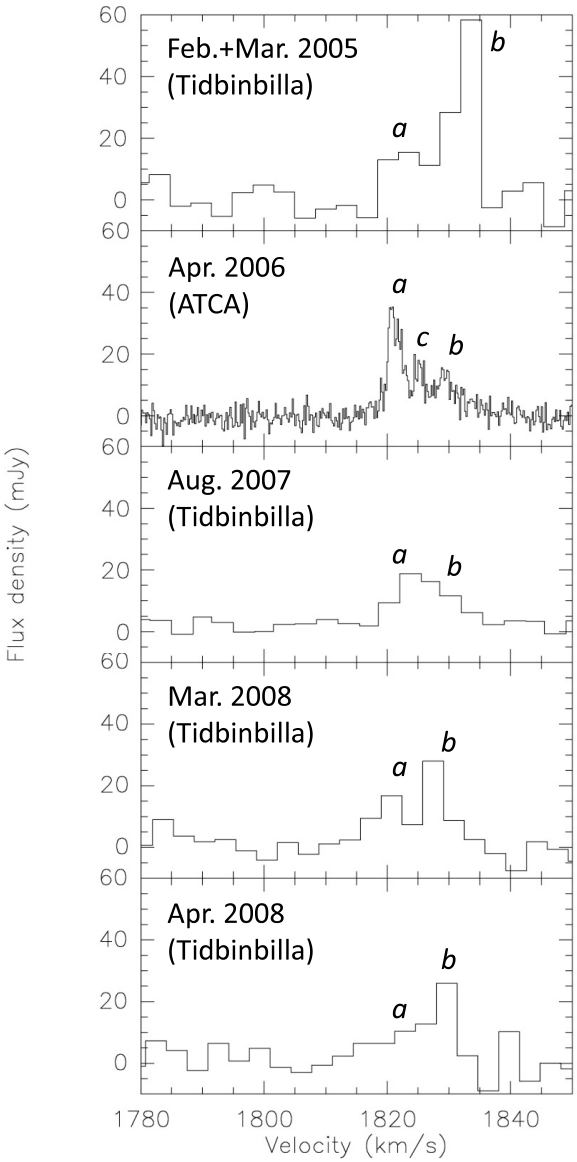

Fig. 3. H_2O spectra observed toward NGC 3620 between February 2005 and April 2008. Channel spacings are 3.4 km s^{-1} (Tidbinbilla) and 0.2 km s^{-1} (ATCA). The pointing position is α_{2000} = 11^{h}16^{m}04^s.7, δ_{2000} = −76°12′59″. The velocity scale is with respect to the local standard of rest (LSR). The recessional LSR velocity of the galaxy is 1691 km s^{-1} according to the NASA/IPAC database (NED).

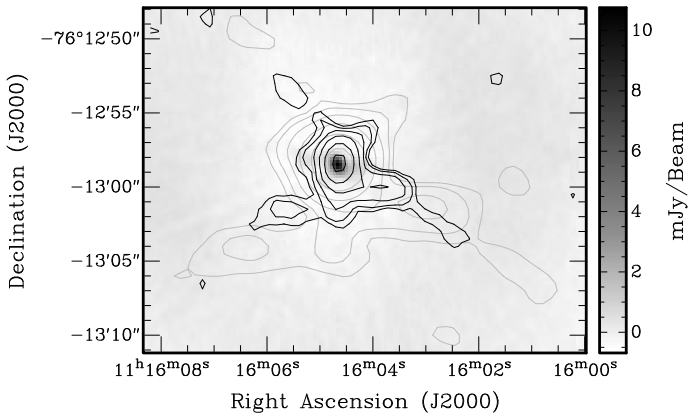

Fig. 4. Radio continuum maps of the nuclear region of NGC 3620, observed with ATCA. *C*-band (4.8 GHz) emission is shown in grey contours, *X*-band (8.6 GHz) emission in black contours, and *K*-band (19.5 GHz) emission, confined toward the nucleus, in grey scale. *C*- and *X*-band contour levels are $3\sigma\times-1, 1, 2, 4, 8, 16, 32, 64$ with σ = 0.4 and 0.2 mJy/beam, respectively. For more details see Tables 3 and 4.

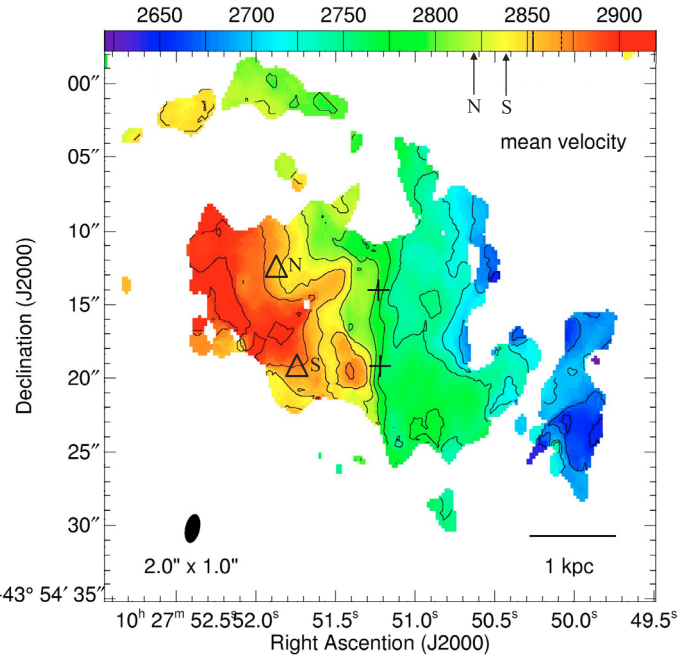

Fig. 5. High-resolution ^{12}CO (2–1) map of the mean velocity in units of km s^{-1} toward the nuclear region of NGC 3256 (Sakamoto et al. 2006, their Fig. 4b). Triangles indicate the positions of the water maser spots found by ATCA (Fig. 2) and the crosses indicate the positions of the two nuclei.

3.1.1. Nuclear continuum emission

To associate the H_2O maser with the main centres of radio emission, an interferometric radio continuum map of NGC 3256 has been produced at 19.5 GHz (see Sect. 2.2).

The map (Fig. 2) shows the two nuclei already observed by NF95 with ATCA at 5 and 8 GHz and by Neff et al. (2003) with the VLA at 5, 8, and 15 GHz. In our *K*-band image, the projected separation between the nuclei is 5.″2 ± 0.″1, consistent with that of NF95. The emission is slightly resolved and the continuum emission of both nuclei, which is more evident in the northern one, shows an elongation toward the south-west. Weaker emission "bridging" the two nuclei is visible. Our map is very similar to those of NF95.

The integrated flux density of the northern nucleus is 6.41 mJy and its position is α_{2000} = 10^{h}27^{m}51^s.23, δ_{2000} = −43°54′14.″0. The southern nucleus exhibits an integrated flux of ∼4.90 mJy at a position of α_{2000} = 10^{h}27^{m}51^s.22, δ_{2000} = −43°54′19.″2 (see Table 3).

Based on their 5 and 8 GHz data, NF95 reported spectral indices for the nuclei of α_N = −0.78 and α_S = −0.86. The spectral indices calculated by including our 19.5 GHz data (after a proper convolution at the 5 GHz beam) are steeper, viz. α_N = −1.22 and α_S = −1.05. They are, however, still indicative of optically thin synchrotron emission as suggested by NF95.

3.2. NGC 3620

NGC 3620 is a peculiar southern SB galaxy (Elfhag et al. 1996). Located at a distance of ∼20 Mpc (1″ ∼ 100 pc;

Table 2. Line parameters of newly detected masers.

Source	D^a (Mpc)	Epoch	Tel.	$\int S\,dV^b$ (mJy km s^{-1})	$V^b_{\rm LSR,opt}$ (km s^{-1})	$\Delta V^b_{1/2}$ (km s^{-1})	V-range (km s^{-1})	Channel Width (km s^{-1})	rms (mJy)	$L^c_{\rm H_2O}$ ($L_\odot$)
NGC 3256	37.4	Aug. 2007	Tid	315	2827 ± 6	63 ± 14	2065, 3407	0.5	3	10.9
		Apr. 2008	ATCA	27.0	2822.1 ± 0.9	7.7 ± 2.3	2611, 2878	3.7	4	1.0
				32.8	2840.2 ± 2.4	15.6 ± 6.3			7	2.4
		Apr. 2008	Tid	400	2797 ± 2	40.0^d	2067, 3409	0.5	3	12.9
NGC 3620	22.4	Feb.–March 2005	Tid	150	1823^d	10.0^d	1000, 2346	0.5	7	4.7^e
				255.2	1833^d	4.4 ± 0.5				
		Apr. 2006	ATCA	71.3	1821.1 ± 0.1	2.5 ± 0.2	1777, 1854	0.2	3	2.1^f
				12.7	1825.1 ± 0.1	1.4 ± 0.4				
				97.2	1827.4 ± 0.8	12.3 ± 1.4				
		Aug. 2007	Tid	376	1826.1 ± 0.8	20.0^d	952, 2298	0.5	3	4.3
		Mar. 2008	Tid	103.7	1820^d	6.1 ± 1.7	1385, 2245	0.5	5	3.2^e
				124.7	1828^d	4.3 ± 0.8				
		Apr. 2008	Tid	114.4	1817.5 ± 3.4	10.4 ± 6.8	994, 2339	0.5	5	2.5^e
				98.8	1824.7 ± 0.8	3.8 ± 2.6				

[a] Distances have been estimated by using velocities taken from the NASA/IPAC Extragalactic Database (NED) and adopting a Hubble constant of $H_0 = 75$ km s^{-1} Mpc^{-1}.
[b] Integrated flux densities, centre velocities, and full width to half maximum (*FWHM*) linewidths of the observed features are obtained from Gaussian fits.
[c] Isotropic luminosities are derived from $L_{\rm H_2O}/[L_\odot] = 0.023 \times \int S\,dV/[\rm Jy\ km\ s^{-1}] \times D^2/[\rm Mpc^2]$.
[d] Values obtained by forcing the fit.
[e] The water maser emission consists of two features.
[f] The water maser emission consists of three features.

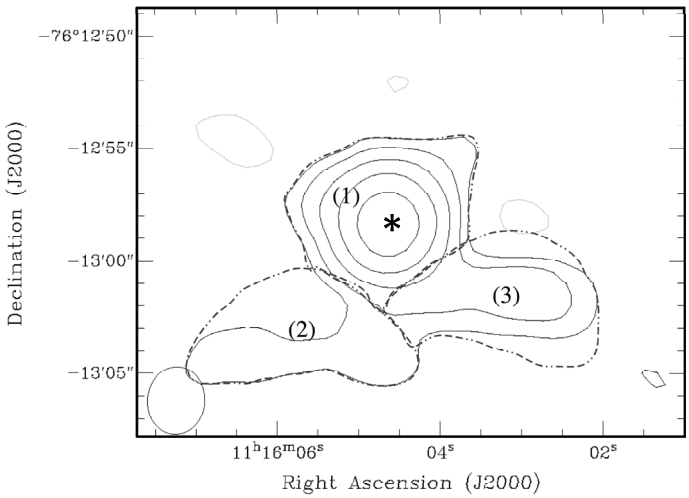

Fig. 6. Radio continuum map of the nuclear region of NGC 3620 at 4.8 GHz. Contour levels are 1.2 mJy/beam × −1 (grey contours), 1, 2, 4, 8, 16, 32 (black contours). The asterisk (in the centre of the map) marks the ATCA position of the H_2O kilomaser. Three regions are indicated by dash-dash-dot-dotted lines: (1) the central emission, (2) the southeastern emission, and (3) the southwestern emission. The beam is shown at the lower left corner.

$H_0 = 75$ km s^{-1} Mpc^{-1}), it shows a significant velocity gradient across the nucleus in optical lines (H_α, [NII], and [SII]), which is probably caused by a rotating disk of gas (Schwartz 1978). There is good agreement between the two optical velocity components, 2.″5 east and west of the nucleus (1649 ± 9 and 1930 ± 33 km s^{-1}, respectively; Schwartz 1978), and the values of the two major peaks in the CO profile (Elfhag et al. 1996). The FIR luminosity is $\sim 4 \times 10^{10}$ $L_\odot$ (Sanders et al. 2003) and the LSR systemic velocity is 1691 km s^{-1}. Neither OH (Staveley-Smith et al. 1992) megamasers nor methanol masers (Phillips et al. 1998) have been detected in NGC 3620.

In February 2005, we detected an H_2O maser in NGC 3620, which was monitored until April 2008. The maser emission consists of two main spectral features (see Fig. 3), denoted "a" ($V_{\rm LSR} \sim 1823$ km s^{-1}) and "b" ($V_{\rm LSR} \sim 1833$ km s^{-1}). Both features are redshifted with respect to the systemic LSR velocity of the galaxy (1691 km s^{-1}). The total isotropic maser luminosity is ∼4.7 $L_\odot$.

In the more sensitive ATCA observation completed in April 2006, the two features, *a* and *b*, were confirmed, and a third feature (hereafter *c*) appeared to be present between these two main ones, possibly detected because of the higher sensitivity and velocity resolution of the spectrum (see Fig. 3). The LSR peak velocity of feature *c* is 1825 km s^{-1}. Details of the results obtained with these ATCA spectral observations are summarised in Table 2. All three maser components originate in a spatially unresolved spot at $\alpha_{2000} = 11^{\rm h}16^{\rm m}04\overset{\rm s}{.}640 \pm 0\overset{\rm s}{.}003$ and $\delta_{2000} = -76°12'58\overset{''}{.}40 \pm 0\overset{''}{.}01$. The total isotropic maser luminosity is ∼2.1 $L_\odot$.

While maser emission is present in all spectra, the relative intensities of the individual features vary drastically. In the 2005 spectrum, feature *b* is dominant with respect to feature *a*. This situation rapidly changes in the later spectra. In the most recent measurements the strength of feature *b* is once again higher.

3.2.1. Nuclear continuum emission

Interferometric radio continuum maps of NGC 3620 have not yet been reported. Hence, to improve our understanding of the central region of the galaxy and, possibly, associate the newly detected H_2O maser with a nucleus, we obtained radio continuum maps at three frequencies. Figure 4 shows the ATCA images of the central region taken at 4.8, 8.6, and 19.5 GHz (details of these maps are given in Tables 3 and 4).

Table 3. Observing parameters for the interferometric continuum maps of NGC 3256 and NGC 3620.

Source	Band	ν (GHz)	Observation date	Telescope	Weighting	Restoring Beam *FWHM* (″)	Position Angle (°)	rms (mJy/beam)
NGC 3256	*K*	19.5	12-Apr.-2008 13-Apr.-2008	ATCA	Natural	1.19×0.59	4.0	0.1
	K[a]	22.1	12-Apr.-2008 13-Apr.-2008	ATCA	Natural	1.16×0.53	6.9	0.2
NGC 3620	*C*	4.8	14-Apr.-2006	ATCA	Natural	2.98×2.51	–4.6	0.4
	X	8.6	14-Apr.-2006	ATCA	Natural	1.92×1.50	–6.2	0.2
	K	19.5	15-Apr.-2006 16-Apr.-2006	ATCA	Natural	0.91×0.61	12.1	0.2
	K[a]	22.1	15-Apr.-2006 16-Apr.-2006	ATCA	Natural	0.85×0.56	7.8	0.2

[a] Obtained by the line-free channels of our *K*-band data at 22 GHz.

Table 4. Gaussian fit parameters of the continuum maps.

Galaxy		Band	Peak flux density (mJy/beam)	Integrated flux density (mJy)	rms (mJy)
NGC3256	(N)	*K*	2.36 ± 0.12	6.41	0.1
	(S)		3.37 ± 0.18	4.90	
NGC3620		*C*	45.96 ± 0.60	73.94[a]	0.4
		X	21.48 ± 0.29	49.02[a]	0.2
		K	10.05 ± 0.30	29.34[a]	0.2
		K[b]	7.12 ± 0.27	16.81[a]	0.2

[a] Obtained by Gaussian fits of maps restored using the beam at 4.8 GHz.
[b] Obtained by subtracting line channels from spectral data at 22 GHz.

Peak intensity positions at the different wavelengths all coincide at $\alpha_{2000} = 11^h16^m04\overset{s}{.}7$ and $\delta_{2000} = -76°12'58\overset{''}{.}33$. The *C*-band emission (Fig. 4, in grey contours) is resolved into a compact nuclear part and some diffuse emission stretching toward the southwestern and southeastern directions. A similar morphology is also observed at 8.6 GHz. *K*-band emission (19.5 GHz, in grey scale), in contrast, is more compact.

A *K*-band (22 GHz) continuum map from the ATCA data cube was produced using only the line-free channels. The position of the peak emission (~7 mJy beam^{-1}) is coincident with the peak of the broad-band ATCA continuum map at 19.5 GHz (Fig. 4) and, more importantly, coincident with that of the maser spot within an overall positional accuracy of ~1″, which was obtained from the quadratic sum of the uncertainties in our line and continuum positions.

4. Discussion

4.1. The nature of the masers in NGC 3256 and NGC 3620

The southern sample (Dec < −30°) targets with FIR 100 μm flux density $S_{100\,\mu m} > 50$ Jy consists of 20 galaxies. Water maser emission was detected in three galaxies: NGC 4945 (Dos Santos & Lèpine 1979) and NGC 3256 and NGC 3620 (Sect. 3).

NGC 3256: The $L_{H_2O} \sim 11\ L_\odot$ maser emission detected at Tidbinbilla is resolved by ATCA into two spots of luminosity 1.0 $L_\odot$ (N) and 2.4 $L_\odot$ (S) (Figs. 1 and 2). Since the sum of the luminosities of the two maser hotspots is insufficient to account for the single dish flux, the single-dish emission must be the result of a superposition of several undetected maser hotspots of which only the two strongest have been detected at high resolution. This situation is similar to that encounterd in NGC 2146 by Tarchi et al. (2002).

Sakamoto et al. (2006) studied the gas kinematics around each nucleus at high-resolution. Comparing our maser velocities with those of their ^{12}CO (2–1) map, we find agreement with the galaxy kinematics (Fig. 5). Both masers are located eastward of the double nucleus and are red-shifted with respect to the systemic velocity (e.g., English et al. 2003). When the velocities of the two maser lines are compared with those of the neighbouring CO gas, the discrepancies are of the order of 25 km s^{-1}, which may represent the local motions of the masing gas. Hence, the H_2O kilomasers in NGC 3256 are not associated with either one of the two nuclei but with the main gas disk hosting an ongoing starburst (Sakamoto et al. 2006).

NGC 3620: The kilomaser emission in NGC 3620 is close to the nuclear region of the galaxy (indicated by an asterisk in Fig. 6). The swap of the two main line features between 2005 and 2006 and the subsequent swap-back in the following epochs appears to imply that there is an anticorrelation between the maser features associated with an accretion disk such as the one in the galactic star-forming region S255 (Cesaroni 1990). To be able to confirm an association of the kilomaser with either a star-forming region or the nucleus of the galaxy, we need to search for a so far undetected Low Luminosity AGN (see Sect. 4.1.1).

4.1.1. What is the nuclear source in NGC 3620?

The spectral index was computed from the three ATCA maps produced at 4.8, 8.6, and 19.5 GHz by fitting the three points in the diagram (ν, S_ν), using the convention $S \propto \nu^\alpha$. The resolutions of the maps are different and range from ~2 arcsec to ~0.5 arcsec. Therefore, a convolution to the same 2 arcsec beam (that at 4.8 GHz) was necessary. The computed spectral indices derived from peak and integrated flux densities (see Table 4) are −1.07 and −0.65, respectively. These values indicate that the radio emission is most likely dominated by optically thin synchrotron emission typical of a collection of sources related to star formation activity such as radio supernovae (RSNs) and supernova remnants (SNRs). Hence, the nuclear region of NGC 3620 is linked to intense star formation, and, apparently, there is no evidence of an AGN (whose spectral index may be flatter) in the centre of the galaxy. However, the spectrum might be artificially steepened by missing flux at higher frequencies. Furthermore, when the nuclear radio continuum emission is divided into three

sub-regions, (1) the central emission, (2) the southeastern emission, and (3) the southwestern emission, the spectral indices, computed by using the integrated flux densities, of the three regions differ slightly. In particular, region (1) has a flatter spectral index ($\alpha_1 = -0.64$) than those of regions (2) and (3) ($\alpha_2 = -2.22$ and $\alpha_3 = -1.54$, respectively). While this is not unusual and can be justified in several other ways, the possibility exists that this is caused by a nuclear component with a flatter or inverted spectral index. Moreover, since the angular resolution of our observation is low (2″ correspond to 200 pc), the lower limit to the brightness temperature in region (1) at X-band ($T_B \geq 10^2$ K) does not allow us to decide between a thermal or non-thermal nature of the central region. Continuum Long Baseline Array (LBA) observations of NGC 3620 at 1.6 GHz have been accepted and await scheduling. This aims to (1) identify nuclear radio continuum sources with particularly high brightness temperature, (2) locate with higher accuracy the radio continuum emission with respect to the maser spot and hence, (3) establishe whether the maser is associated with star formation as for the majority of kilomasers or, if present, with AGN activity.

4.2. Statistical considerations

The detection rate in the southern sample is 3/20 or, applying the Bernoulli theorem, (15 ± 8)%. Since the rms values of the northern and southern samples are comparable (see Table 5) because of the different integration times, this detection rate is compatible with that obtained by HPT, i.e., (22 ± 6)%. Braatz & Gugliucci (2008) found a water kilomaser in NGC 4527, which remained undetected by HPT. Darling et al. (2008) also reported the detection of a new water kilomaser in the Antennae system consisting of two galaxies, NGC 4038 and NGC 4039. This demonstrates that the high sensitivity of the Green Bank Telescope (GBT) is capable of increasing the number of detected kilomasers in our sample (see below). With these new detections, the northern detection rate becomes (27 ± 7)% (12/45).

Adding the southern sources, the complete all-sky sample with $S_{100\,\mu m} > 50$ Jy finally consists of 65 galaxies (Table 5). Among them, water maser emission was detected in 15 galaxies. There are 10 kilomasers (IC 10, NGC 253, IC 342, NGC 2146, M 82, NGC 3556, NGC 3620, NGC 4038/9, NGC 5194, and NGC 4527), 4 megamasers (NGC 1068, Arp 299, NGC 3079, and NGC 4945), and one maser (NGC 3256) with an isotropic luminosity just above the 10 $L_\odot$ threshold conventionally used to discriminate between megamasers and kilomasers. Since the maser emission is associated with sites of massive star formation and since the individual ATCA maser spots have luminosities well below the 10 $L_\odot$ threshold, NGC 3256 is also a kilomaser source. As already mentioned in Sect. 1, the majority of the kilomasers are associated with star formation. Most of them contain a collection of Galactic-type masers related to (pre-) stellar activity. Therefore, a relation between kilomasers and FIR emission is readily explained, since the latter commonly originates in warm dust grains heated by young massive stars. The bulk of the 22 GHz H_2O emission from the four megamasers in our sample (NGC 1068, NGC 3079 and NGC 4945 but presumably not Arp 299) is associated with nuclear accretion disks surrounding an AGN (Gallimore et al. 1997; Greenhill et al. 1997; Trotter et al. 1998; Tarchi et al. 2007).

In our complete sample, 40% (6/15) of the water masers were detected in galaxies classified as Seyfert, all of type 2 (see Table 5). The other 9 masers are detected in spiral galaxies (27%, 4/15), merger systems (20%, 3/15), LINERs (7%, 1/15), and the last one in a starburst galaxy (7%, 1/15).

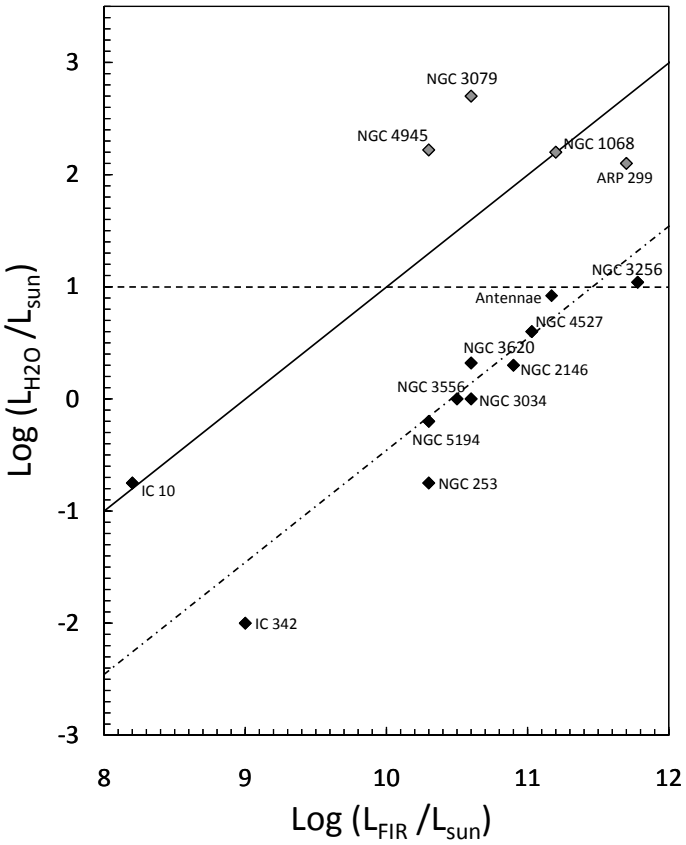

Fig. 7. H_2O vs. FIR luminosity including the 15 masers of the complete all-sky FIR-sample, and the line separating between the kilomaser and megamaser regimes for H_2O masers (dashed horizontal line). The solid line shows the correlation found by Jaffe et al. (1981) for Galactic sources ($\log(L_{H_2O}) = \log(L_{FIR}) - 9$). The dot-dashed diagonal line shows the FIR/H_2O luminosity relation for the kilomaser sources ($\log(L_{H_2O}) = \log(L_{FIR}) - 10.4$), with the slope being fixed to that of the Jaffe et al. (1981) correlation. Black diamonds denote kilomasers, grey diamonds mark megamasers. The figure is a modified version of Fig. 6 of CTH.

The high rate of maser detections in the complete all-sky sample (23%, 15/65) confirms the link between FIR flux density and maser phenomena as suggested previously by HPT and CTH. In particular, the detection rate strongly declines with decreasing FIR flux. Adding the masers detected in the southern sample to those of HPT, for fluxes of 300−1000 Jy, 100−300 Jy, and 50−100 Jy, we find detection rates of 3/4 or 75%, 6/21 or 29%, and 6/40 or 15%.

HPT found a proportionality between L_{FIR} and L_{H_2O} for extragalactic water masers, which is surprisingly consistent with that obtained for the orders of magnitude less luminous Galactic sources of Jaffe et al. (1981). Furthermore, CTH observed that megamaser and kilomaser sources seem to follow independent correlations (the two samples diverge by ∼1.5 orders of magnitude in maser luminosity for a given FIR luminosity), with the tighter one being that for kilomasers. In Fig. 7, we plot the values for the masers of the complete all-sky FIR-sample including the known maser in NGC 4945 and the most recent detections in NGC 3256, NGC 3620, NGC 4527 ($L_{FIR} \sim 1 \times 10^{11}$ $L_\odot$) and the Antennae ($L_{FIR} \sim 1.5 \times 10^{11}$ $L_\odot$). The luminosities of the kilomasers in our all-sky sample follow the trend given by $\log(L_{H_2O}) = \log(L_{FIR}) - 10.4$. The most discrepant point is that representing IC 10, which is also peculiar in its number of water masers as pointed out by Brunthaler et al. (2006). Overall,

Table 5. The complete all-sky FIR sample.

Source[a]	Classification[b]	RA[b] (J2000)	Dec[b] (J2000)	V^b_{sys} (km s^{-1})	$S^c_{100\,\mu m}$ (Jy)	rms (mJy)	$L^d_{H_2O}$ ($L_\odot$)	L^d_{OH} ($L_\odot$)	Ref.[e]
NGC 0055	SB(s)m:sp	00h14m53.6s	–39d11m48s	+149	78	10	<0.001	<0.004	w1, h1
IC 10	dIrr IV/BCD	00h20m17.3s	+59d18m14s	–358	71	16	0.18	<0.004	w2, h2
NGC 0134	SAB(s)bc HII	00h30m22.0s	–33d14m39s	+1598	57	5	<0.08	<0.21	w2, h1
NGC 0253	SAB(s)c;Sbrst Sy2 HII	00h47m33.1s	–25d17m18s	+251	1045	10	0.18	0.1	w2, h3, h6
NGC 0300	SA(s)d	00h54m53.5s	–37d41m04s	+152	75	9	<0.001	–	w1
NGC 0660	SB(s)a pec; HII LINER	01h43m02.4s	+13d38m42s	+838	104	10	<0.07	–	w2
NGC 0891	SA(s)b? sp HII	02h22m33.4s	+42d20m57s	+548	148	20	<0.08	<0.004	w2, h2
NGC 0972	Sab HII	02h34m13.4s	+29d18m41s	+1555	65	10	<0.65	–	w2
NGC 1055	SBb; sp; Sy2 LINER	02h41m45.2s	+00d26m35s	+989	60	17	<0.23	<0.008	w2, h4
Maffei 2	SAB(rs)bc:	02h41m55.1s	+59d36m15s	–23	227	17	<0.0001	–	w2
NGC 1068	SA(rs)b;Sy1 Sy2	02h42m40.7s	–00d00m48s	+1131	240	40	158	0.83	w2, h5
NGC 1084	SA(s)c HII	02h45m59.9s	–07d34m43s	+1427	55	20	<0.55	<0.13	w2, h2
NGC 1097	SB(r'1)b Sy1	02h46m19.0s	–30d16m30s	+1253	85	15	<0.30	<0.05	w1, h6
NGC 1313	SB(s)d HII	03h18m16.0s	–66d29m54s	+456	92	4	<0.005	–	w1
NGC 1365	SBb(s)b;HII Sy1.8	03h33m36.4s	–38d08m25s	+1616	142	12	<0.39	<0.20	w1, h1
IC 342	SAB(rs)cd; Sy2 HII	03h46m48.5s	+68d05m46s	+49	128	12	0.01	<0.002	w2, h3
UGC 02855	SABc	03h48m20.7s	+70d07m58s	+1186	79	9	<0.17	<0.03	w2, h2
NGC 1559	SB(s)cd	04h17m35.8s	–62d47m01s	+1307	56	5	<0.05	<0.10	w1, h1
NGC 1569	IBm;Sbrst Sy1	04h30m49.0s	+64d50m53s	–122	52	12	<0.002	<0.0007	w2, h2
NGC 1672	SB(r)bc Sy2	04h45m42.5s	–59d14m50s	+1339	70	19	<0.41	<0.11	w1, h1
NGC 1792	SA(rs)bc	05h05m14.4s	–37d58m51s	+1221	77	5	<0.05	–	w1
NGC 1808	SAB(s:)b Sy2	05h07m42.3s	–37d30m47s	+995	137	15	<0.18	<0.05	w1, h7
NGC 2146	SB(s)ab pec HII	06h18m37.7s	+78d21m25s	+891	187	7	2	<0.02	w2, h2, h6
NGC 2403	SAB(s)cd HII	07h36m51.4s	+65d36m09s	+123	56	9	<0.002	<0.0003	w2, h2
NGC 2559	SB(s)bc pec:	08h17m06.1s	–27d27m21s	+1576	66	20	<0.67	–	w2
NGC 2903	SB(s)d HII	09h32m10.1s	+21d30m03s	+553	104	7	<0.03	<0.01	w2, h2, h6
NGC 2997	SA(s)c	09h45m38.8s	–31d11m28s	+1081	85	7	<0.05	–	w1
NGC 3034 (M 82)	I0;Sbrst HII	09h55m52.7s	+69d40m46s	+287	1145	20	1	0.1	w2, h3, h6
NGC 3079	SB(s)c;LINER Sy2	10h01m57.8s	+55d40m47s	+1128	89	40	501	0.07	w2, h8
NGC 3256	Pec;merger;HII Sbrst	10h27m51.3s	–43d54m14s	+2799	115	7	10.9	<0.02	w1, h1
NGC 3521	SAB(rs)bc;HII LINER	11h05m48.6s	–00d02m09s	+795	85	29	<0.25	–	w2
NGC 3556	SB(s)cd HII	11h11m31.0s	+55d40m27s	+708	61	10	1	<0.03	w2, h6
NGC 3620	SB(s)ab	11h16m04.7s	–76d12m59s	+1691	66	7	2.1	<0.004	w1, h7
NGC 3621	SA(s)d HII	11h18m16.5s	–32d48m51s	+749	61	5	<0.02	<0.05	w1, h1
NGC 3627	SAB(s)b;LINER Sy2	11h20m15.0s	+12d59m30s	+716	106	8	<0.21	<0.01	w2, h6
NGC 3628	SAb pec sp;HII LINER	11h20m17.0s	+13d35m23s	+825	103	7	<0.25	–	w2
Arp 299	merger	11h28m30.4s	+58d34m10s	+3073	111	5	126	13	w2, w3, h3
NGC 4038	SB(s)m pec,merger	12h01m53.0s	–18d52m10s	+1634	76	28	8.2	<0.07	w4, h1
NGC 4088	SAB(rs)bc HII	12h05m34.2s	+50d32m21s	+746	52	16	<0.12	–	w2
NGC 4102	SAB(s)b?;HII LINER	12h06m23.1s	+52d42m39s	+838	69	17	<0.16	<0.02	w2, h2
NGC 4254	SA(s)c	12h18m49.6s	+14d24m59s	+2390	72	6	<1.81	–	w2
NGC 4303	SAB(rs)bc;HII Sy2	12h21m54.9s	+04d28m25s	+1586	62	13	<0.44	–	w2
NGC 4321	SAB(s)bc;LINER HII	12h22m54.9s	+15d49m21s	+1581	58	12	<0.41	<0.02	w2, h4
NGC 4414	SA(rs)c?;HII LINER	12h26m27.1s	+31d13m25s	+711	68	17	<0.12	<0.007	w2, h4
NGC 4490	SB(s)d pec	12h30m36.4s	+41d38m37s	+583	78	17	<0.08	<0.01	w2, h2
NGC 4501	SA(rs)b;HII Sy2	12h31m59.2s	+14d25m14s	+2264	55	10	<0.69	–	w2
NGC 4527	SAB(s)bc;HII LINER	12h34m08.5s	+02d39m14s	+1730	64	15	4	–	w5
NGC 4631	SB(s)d	12h42m08.0s	+32d32m29s	+687	120	7	<0.17	<0.005	w2, h4
NGC 4666	SABc;HII LINER	12h45m08.6s	–00d27m43s	+1524	77	10	<0.31	–	w2
NGC 4736	SA(r)ab;Sy2 LINER	12h50m53.0s	+41d07m14s	+321	105	5	<0.03	<0.004	w2, h2
NGC 4826	SA(rs)ab;HII Sy2	12h56m43.7s	+21d40m58s	+407	76	11	<0.03	<0.004	w2, h6
NGC 4945	SB(s)cd: sp Sy2	13h05m27.5s	–49d28m06s	+547	620	–	165	<0.03	w6, h7
NGC 5005	SAB(rs)bc;Sy2 LINER	13h10m56.2s	+37d03m33s	+952	59	13	<0.16	–	w2
NGC 5055	SA(rs)bc HII/LINER	13h15m49.3s	+42d01m45s	+524	101	12	<0.05	<0.008	w2, h2
NGC 5128 (Cen A)	S0 pec Sy2	13h25m27.6s	–43d01m09s	+529	314	2	<0.02	–	w1
NGC 5194	SA(s)bc pec;HII Sy2.5	13h29m52.7s	+47d11m43s	+467	123	10	0.63	<0.01	w2, h2
NGC 5236	SAB(s)c;HII Sbrst	13h37m00.9s	–29d51m56s	+494	213	34	<0.11	<0.01	w2, h6
Arp 220	merger	15h34m57.1s	+23d30m11s	+5454	118	10	<4.01	580	w2, h3, h9
NGC 6000	SB(s)bc:;HII Sbrst	15h49m49.5s	–29d23m13s	+2178	59	25	<1.60	<0.06	w2, h7
NGC 6744	SAB(r)bc LINER	19h09m46.1s	–63d51m27s	+857	86	15	<0.13	–	w1
NGC 6946	SAB(rs)cd;Sy2 HII	20h34m52.3s	+60d09m14s	+51	128	11	<0.0004	<0.00007	w2, h2

Table 5. continued.

Source[a]	Classification[b]	RA[b] (J2000)	Dec[b] (J2000)	V^b_{sys} (km s^{-1})	$S^c_{100\,\mu m}$ (Jy)	rms (mJy)	$L^d_{H_2O}$ ($L_\odot$)	L^d_{OH} ($L_\odot$)	Ref.[e]
NGC 7331	SA(s)b LINER	22h37m04.1s	+34d24m56s	+806	82	14	<0.12	<0.02	w2, h2
NGC 7552	SB(s)ab;HII LINER	23h16m10.8s	–42d35m05s	+1628	102	13	<0.41	<0.05	w1, h7
NGC 7582	SB(s)ab Sy2	23h18m23.5s	–42d22m14s	+1555	73	13	<0.40	<0.12	w1, h1
NGC 7793	SA(s)d HII	23h57m49.8s	–32d35m28s	+247	56	7	<0.002	–	w1

[a] Source names with detected H_2O masers are presented boldfaced.
[b] Classification, coordinates and LSR velocities are taken from the NASA/IPAC Extragalactic Database (NED).
[c] Flux densities at 100 μm are taken from the IRAS Point Source Catalog (Fullmer & Lonsdale 1989).
[d] Isotropic luminosity thresholds are derived from $L/[L_\odot] = k \times S/[\mathrm{Jy}] \times \Delta v/[\mathrm{km\ s^{-1}}] \times D^2/[\mathrm{Mpc^2}]$, where k is 0.023 and 0.0017 for H_2O and OH masers respectively.
[e] References: (w1) present work; (w2) HPT; (w3) Tarchi et al. (2007); (w4) Darling et al. (2008); (w5) Braatz & Gugliucci (2008); (w6) Dos Santos & Lèpine (1979); (h1) Norris et al. (1989); (h2) Baan et al. (1992); (h3) Staveley-Smith et al. (1987); (h4) Schmelz & Baan (1988); (h5) Gallimore et al. (1996); (h6) Unger et al. (1986); (h7) Staveley-Smith et al. (1992); (h8) Baan & Irwin (1995); (h9) Baan et al. (1982).

the water kilomasers in our all-sky FIR-sample reinforce the L_{FIR}/L_{H_2O} correlation for kilomasers found by CTH.

4.2.1. GBT and EVLA: how many more masers could be detected in FIR-sample?

The entire sample of FIR bright ($S_{100\,\mu m} > 50$ Jy) galaxies was observed with three different telescopes, the 100-m Effelsberg, the 70-m Tidbinbilla, and the 100-m Green Bank telescope (GBT). Each telescope has a different sensitivity at 22 GHz, i.e. 0.83[4], 0.67[5], and 1.50 K/Jy (Minter 2009), using an antenna temperature scale (T^*_A), with respect to a point source. For this study, the smaller size of the Tidbinbilla telescope was compensated for by longer integration times with respect to the Effelsberg telescope (see Table 5).

Future observations of higher sensitivity with the GBT and EVLA will likely lead to new detections. It is therefore of interest to evaluate this increase in the number of water masers. The evaluation can be made by considering the standard equation of the water maser density as reported by HPT for a specific slope of the luminosity function (γ_{SLF}, about –1.5, see below), that is

$$N_{H_2O} = C_1 L^{\gamma_{SLF}}_{H_2O}. \quad (2)$$

The integration of Eq. (2) from a minimum luminosity, determined by the sensitivity of the radio telescope, to infinity gives

$$N_{tot} = -\frac{C_1}{\gamma_{SLF}+1} L^{\gamma_{SLF}+1}_{min} = C_2\, L^{\gamma_{SLF}+1}_{min}. \quad (3)$$

Rewriting Eq. (3) for the GBT and the Effelsberg/Tidbinbilla (ET) radio telescopes, we obtain

$$N_{ET} = C_2\, L^{\gamma_{SLF}+1}_{min,ET}, \qquad N_{GBT} = C_2\, L^{\gamma_{SLF}+1}_{min,GBT}. \quad (4)$$

With τ being the ratio of the ET to the GBT sensitivity, we then obtain from Eqs. (4)

$$N_{GBT} = C_2\, (\tau)^{\gamma_{SLF}+1}\ L^{\gamma_{SLF}+1}_{min,ET}. \quad (5)$$

The ratio of the GBT to ET total number of detectable masers is

$$\frac{N_{GBT}}{N_{ET}} = (\tau)^{\gamma_{SLF}+1} \simeq 1.4, \quad (6)$$

where we have assumed $\tau = 0.55$ and $\gamma_{SLF} = -1.5$ (HPT, Bennert et al. 2009). Assuming that the EVLA sensitivity will be 2.44 K/Jy[6] (Perley et al. 2006),

$$\frac{N_{EVLA}}{N_{ET}} \simeq 1.7. \quad (7)$$

Since the number of masers in the FIR-sample is 13 (considering only those detected using the ET radio telescopes), by performing a survey on the same sample with the GBT and the EVLA, with an observing time comparable with that used in our survey with Effelsberg, we expect to obtain 5 and 9 new maser detections, respectively. Two new detections of sources belonging also to our sample were reported by Braatz & Gugliucci (2008) and Darling et al. (2008). Although the integration times in these surveys with the GBT were shorter than those of our Effelsberg survey, their GBT detection thresholds have confirmed the usefulness of deeper surveys. Hence, in that case the detection rate for the FIR-sample is expected to rise to 28% and 34%, respectively.

4.3. Is there a relation between OH and H_2O maser emission?

Out of the 65 sources of our all-sky FIR sample, searches for $\lambda = 18$ cm hydroxyl (OH) maser emission have been reported for 45 galaxies (i.e. ~70%). In 6 galaxies, OH maser emission was detected (i.e. ~13%). The percentage of galaxies in our sample that have not been searched for OH masers is higher at lower FIR fluxes (about 30% and 40% for $S_{100\,\mu m}$ below 200 and 100 Jy, respectively).

In Fig. 8, both the H_2O (squares) and OH (triangles) total cumulative detection rates above a given 100 μm IRAS Point Source Catalog flux are plotted. The trends are similar. Naturally, these trends also reflect that the surveys involved are sensitivity-limited and have, for the two maser species, different detection thresholds. For H_2O masers, the influence produced by a possible distance bias was extensively discussed in HPT (their Sect. 4.3).

In Fig. 9, we plot maser isotropic luminosities for all sources (45 out of 65) of the all-sky FIR-sample for which H_2O and OH masers have been searched (see also Table 5). Arrows indicate upper limits to the H_2O and/or OH maser luminosity in the case of non-detections (3σ noise level). For example, water maser emission was detected in NGC 4945 with 165 $L_\odot$ (Dos Santos & Lèpine 1979), while it remains undetected, so

[4] www.mpifr-bonn.mpg.de/div/effelsberg/calibration
[5] www.atnf.csiro.au/observers/tidbinbilla
[6] www.gb.nrao.edu/gbt

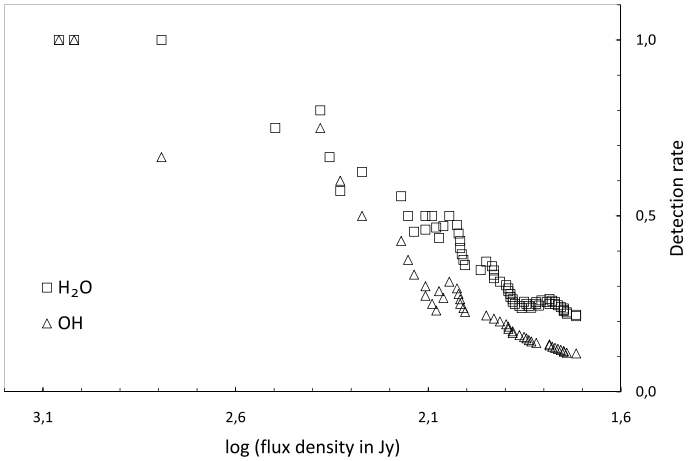

Fig. 8. Total H_2O and OH maser cumulative detection rates above a given IRAS Point Source Catalog $S_{100\,\mu m}$ flux density. The figure is an expanded version of Fig. 13 of HPT, with the data from OH and our sample being included.

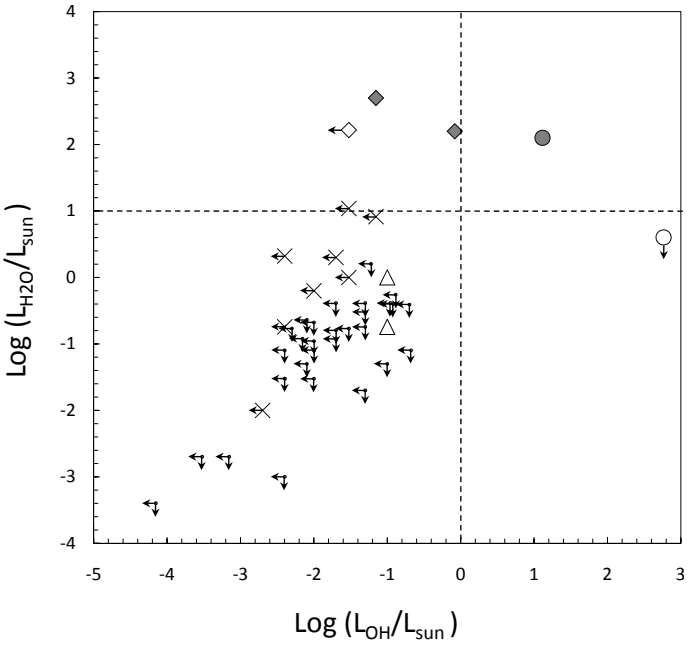

Fig. 9. OH vs. H_2O maser luminosity plot including all sources belonging to the complete all-sky FIR-sample where masers from both species have been searched for. Crosses represent the galaxies hosting only H_2O kilomasers, triangles both H_2O kilomasers and weaker OH masers, diamonds H_2O megamasers, filled diamond both H_2O megamaser and weaker OH maser, circles OH megamasers and the filled circle both H_2O and OH megamasers. For non-detections, the arrow marks the detection luminosity threshold (3σ) of the survey in that maser transition. The dashed lines indicate the separation between kilomaser and megamaser regimes as found in the literature (for H_2O masers, see Sect. 1; for OH masers, see Henkel & Wilson 1990).

far, in $\lambda = 18$ cm OH down to a detection threshold of 0.46 $L_\odot$ (Staveley-Smith et al. 1992). Among the 45 sources, no detection in both maser species has been reported for 31 sources, 14 are H_2O detections, and 6 host OH maser emission. Both maser species have been detected in five galaxies: three water megamaser sources, NGC 1068, NGC 3079, and Arp 299, and two water kilomaser sources, the well-known starburst galaxies NGC 253 and NGC 3034 (M 82).

In Galactic star-forming regions, the two maser species are very often associated with each other, suggesting that the OH and H_2O masers occur near a common energy source but in physically distinct zones (e.g., Forster & Caswell 1989). This is probably due to the diverse excitation and pumping conditions of the respective lines. OH maser emission, excited mostly radiatively and requiring comparatively low density gas, is more extended and farther off the excitation source than the water masers, which are probably collisionally excited and require higher temperature and density (e.g., Lo 2005; Tarchi et al. 2007). Typical angular separations between the two maser group associations in Galactic star-forming regions are of a few arcseconds corresponding to linear separations of $\lesssim$1 parsec at a distance of $\lesssim$10 kpc. Hence, with the relatively coarse resolution of our single-dish surveys, masers of the two species associated with star formation would be seen, if present, in the same beam. This seems indeed to be the case for our sample.

If we consider that six galaxies are detected in OH and assuming that H_2O and OH masers are unrelated phenomena within the sample being considered, we can compute the expected number of those galaxies that should be detected in H_2O. This number is ~1, while, instead, the number in our sample of sources showing both masers is 5. Furthermore, for 31 galaxies, where no OH maser has been detected, H_2O maser emission is also not seen. Therefore, we are inclined to conclude that, as for Galactic sources, an association between H_2O and OH emission does exist for extragalactic targets. Noticeably, with the only exception of Arp 299 (Tarchi et al. 2007), the contemporary presence of megamaser emission[7] from both species has never been reported. This may indicate that while weaker, Galactic-type, H_2O and OH masers are often associated (if not correlated) as in our Galaxy, the presence of most luminous masers of the two species seem to be mutually exclusive.

Given the relatively low number of sources involved, we are aware of the limited statistical relevance of this result. Furthermore, statistics may be affected by the different and/or insufficient sensitivities of maser searches and by the possible variability in the maser features. To provide a more statistically relevant support to our arguments, a more extensive study of a sample of all the detected extragalactic water (~100, Braatz et al. 2007) and/or hydroxyl maser sources (~100, Darling 2007) is advisable. This is, however, outside the scope of the present work and will be the subject of future publication.

5. Conclusions

We have observed 12 sources out of a sample of 20 galaxies with 100 μm IRAS point source flux densities >50 Jy and declination <−30° to search for water maser emission at 22 GHz. Our main results are that:

1. By including the southern galaxies, our complete FIR-sample covers the entire sky.
2. Two new detections were obtained. One is a kilomaser with an isotropic luminosity, L_{H_2O}, of ~5 $L_\odot$ in the SB galaxy NGC 3620. The other is a maser with $L_{H_2O} \sim 11\ L_\odot$ in the merger system NGC 3256.
3. Follow-up interferometric observations of both sources have been performed. In NGC 3256, the maser is resolved into two spots offset from the two nuclei of the system implying an association of the maser with particularly vigorous

[7] The isotropic luminosity typically adopted to discriminate between OH mega and kilomaser sources is 1 $L_\odot$ (Henkel & Wilson 1990), while it is 10 $L_\odot$ for H_2O masers (see Sect. 1).

star formation. For NGC 3620, the maser emission coincides with the nuclear region. In this case, an association with star formation activity is also likely, although an association with a Low Luminosity AGN cannot be a priori ruled out.

4. The high rate of water maser detections in the FIR sample encompassing northern and southern sources (23%, 15/65) confirms a link between FIR flux density and maser phenomena as reported in HPT and CTH. Our results further reinforce the correlation between water masers and FIR luminosities for kilomasers while the correlation with megamasers is weaker. The latter is explained by megamasers in the nuclear region not being related to the overall star forming activity of their parent galaxy. Albeit this awaits a more extensive statistical dataset, an association between H_2O and OH masers in the FIR sample is suggested for sources where at least one of the maser species has weak emission. However, there is no apparent correlation between H_2O and OH megamasers. Given the relatively low number of sources, a systematic study of H_2O megamaser sources in OH, and of OH megamasers in H_2O is highly desirable.

Acknowledgements. We wish to thank Shinji Horiuchi for performing part of the observations at Tidbinbilla and for useful discussions, and an anonymous referee for making useful suggestions. A.T. would like to thank Lincoln Greenhill and Paul Kondratko for helpful suggestions in the early stages of this project, and Alessandro Riggio for his advice on statistics. G.S. would like to thank Wouter Vlemmings for helpful comments. This research has made use of the NASA/IPAC Extragalactic Database (NED), which is operated by the Jet Propulsion Laboratory, Caltech, under contract with NASA. This research has also made use of NASA's Astrophysics Data System Abstract Service (ADS). The National Radio Astronomy Observatory is a facility of the National Science Foundation operated under cooperative agreement by Associated Universities, Inc. G.S. is a Member of the International Max Planck Research School (IMPRS) for Radio and Infrared Astronomy at the Universities of Bonn and Cologne.

References

Baan, W. A., & Irwin, J. A. 1995, ApJ, 446, 602
Baan, W. A., Wood, P. A. D., & Haschick, A. D. 1982, ApJ, 260, L49
Baan, W. A., Haschick, A., & Henkel, C. 1992, AJ, 103, 728
Batchelor, R. A., Jauncey, D. L., & Whiteoak, J. B. 1982, MNRAS, 200, 19
Bennert, N., Barvainis, R., Henkel, C., & Antonucci, R. 2009, ApJ [arXiv:astro-ph/0901.0567]
Böker, T., Storey, J. W. V., Krabbe, A., & Lehmann, T. 1997, PASP, 109, 827
Braatz, J., Kondratko, P., Greenhill, L., et al. 2007, in IAU Symp., 242, 402
Braatz, J. A., & Gugliucci, N. E. 2008, ApJ, 678, 96
Braatz, J. A., Wilson, A. S., & Henkel, C. 1996, ApJS, 106, 51
Braatz, J. A., Wilson, A. S., & Henkel, C. 1997, ApJS, 110, 321
Braatz, J. A., Henkel, C., Greenhill, L. J., et al. 2004, ApJ, 617, 29
Braatz, J. A., Reid, M. J., Greenhill, L. J., et al. 2008, ASPC, 395, 103
Brunthaler, A., Reid, M. J., Falcke, H., et al. 2005, Science, 307, 1440
Brunthaler, A., Henkel, C., de Blok, W. J. G., et al. 2006, A&A, 457, 109
Brunthaler, A., Reid, M. J., Falcke, H., et al. 2007, A&A, 462, 101
Castangia, P., Tarchi, A., Henkel, C., & Menten, K. M. 2008, A&A, 479, 111 (CTH)
Casoli, F., Dupraz, C., Combes, F., & Kazes, I. 1991, A&A, 251, 1
Cesaroni, R. 1990, A&A, 233, 513
Darling, J. 2007, in IAU Symp., 242, 417
Darling, J., Brogan, C., & Johnson, K. 2008, ApJ, 685, 39
de Vaucouleurs, G., & de Vaucouleurs, A. 1961, Mem. R. Astron. Soc., 68, 69
Dos Santos, P. M., & Lèpine, J. R. D. 1979, Nature, 278, 34
Doyon, R., Joseph, R. D., & Wright, G. S. 1994, ApJ, 421, 101
Elfhag, T., Booth, R. S., Höglund, B., et al. 1996, A&AS, 115, 439
English, J., Norris, R. P., Freeman, K. C., & Booth, R. S. 2003, ApJ, 125, 1134
Forster, J. R., & Caswell, J. L. 1989, A&A, 213, 339
Fullmer, L., & Lonsdale, C. 1989, Cataloged Galaxies and Quasars Observed in the IRAS Survey, Version 2, JPL D-1932
Gallimore, J. F., Baum, S. A., O'Dea, C. P., et al. 1996, ApJ, 462, 740
Gallimore, J. F., Baum, S. A., O'Dea, C. P., & Claussen, M. 1997, IAUJD, 21E, 10
Greenhill, L. J., Moran, J. M., & Herrnstein, J. R. 1997, ApJ, 560, L37
Greenhill, L. J., Kondratko, P. T., Lovell, J. E. J., et al. 2003, ApJ, 582, L11
Hagiwara, Y., Henkel, C., Menten, K. M., & Nakai, N. 2001, ApJ, 560, L37
Hagiwara, Y., Diamond, P. J., Miyoshi, M., et al. 2003, MNRAS, 344, L53
Henkel, C., & Wilson, T. L. 1990, A&A, 229, 431
Henkel, C., Wouterloot, J. G. A., & Bally, J. 1986, A&A, 155, 193
Henkel, C., Braatz, J. A., Tarchi, A., et al. 2005a, Ap&SS, 295, 107
Henkel, C., Peck, A. B., Tarchi, A., et al. 2005b, A&A, 436, 75 (HPT)
Herrnstein, J. R., Moran, J. M., Greenhill, L. J., et al. 1999, Nature, 400, 539
Ho, P. T. P., Martin, R. N., Henkel, C., et al. 1987, ApJ, 320, 663
Högbom, J. A. 1974, A&AS, 15, 417
Impellizzeri, C. M. V., Kean, J. P., Castangia, P., et al. 2008, Nature, 456, 927
Jaffe, D. T., Guesten, R., & Downes, D. 1981, ApJ, 250, 621
Jenkins, L. P., Roberts, T. P., Ward, M. J., & Zezas, A. 2004, MNRAS, 352, 1335
Lípari, S., Díaz, R., Taniguchi, Y., et al. 2000, AJ, 120, 645
Lira, P., Ward, M., Zezas, A., et al. 2002, MNRAS, 330, 259
Lira, P., Gonzalez-Corvalan, V., Ward, M., & Hoyer, S. 2008, MNRAS, 384, 316
Lo, K.-Y. 2005, ARA&A, 43, 625
Kondratko, P. T., Greenhill, L. J., Moran, J. M., et al. 2006, ApJ, 638, 100
Kotilainen, J. K., Moorwood, A. F. M., Ward, M. J., & Forbes, D. A. 1996, A&A, 305, 107
Minter, T. 2009, The Proposer's Guide for the Green Bank Telescope
Miyoshi, M., Moran, J., Herrnstein, J. R., et al. 1995, Nature, 373, 127
Neff, S. G., Ulvestad, J. S., & Campion, S. D. 2003, ApJ, 599, 1043
Norris, R. P., & Forbes, D. A. 1995, ApJ, 446, 594 (NF95)
Norris, R. P., Gardner, F. F., Whiteoak, J. B., et al. 1989, MNRAS, 237, 673
Perley, R., Hayward, B., Butler, B., et al. 2006, EVLA memo 103, www.aoc.nrao.edu/evla/geninfo/memoseries
Phillips, C. J., Norris, R. P., Ellingsen, S. P., & Rayner, D. P. 1998, MNRAS, 294, 265
Reid, M. J., Braatz, J. A., Condon, J. J., et al. 2009 [arXiv:astro-ph/0811.4345]
Sakamoto, K., Ho, P. T. P., Peck, A. B., et al. 2006, ApJ, 644, 862
Sanders, D. B., Mazzarella, J. M., Kim, D.-C., et al. 2003, ApJ, 126, 1607
Sargent, A. I., Sanders, D. B., & Phillips, T. G. 1989, ApJ, 346, L9
Schmelz, J. T., & Baan, W. A. 1988, AJ, 95, 672
Schwartz, D. 1978, PASP, 90, 393
Staveley-Smith, L., Cohen, R. J., Chapman, J. M., et al. 1987, MNRAS, 226, 689
Staveley-Smith, L., Norris, R. P., Chapman, J. M., et al. 1992, MNRAS, 258, 725
Tarchi, A., Henkel, C., Peck, A. B., et al. 2002, A&A, 389, 39
Tarchi, A., Castangia, P., Henkel, C., & Menten, K. M. 2007, NewAR, 51, 67
Trotter, A. S., Greenhill, L. J., Moran, J. M., et al. 1998, ApJ, 495, 740
Unger, S. W., Chapman, J. M., Cohen, R. J., et al. 1986, MNRAS, 220, 1